# Growth mechanism and interface magnetic properties of Co nanostructures on graphite

P. K. J. Wong, M. P. de Jong,* L. Leonardus, M. H. Siekman, and W. G. van der Wiel

*NanoElectronics Group, MESA+ Institute for Nanotechnology, University of Twente, P.O. Box 217, 7500 AE Enschede, The Netherlands*

(Received 13 April 2011; published 5 August 2011)

We investigated structural, electronic, and magnetic properties of Co adsorbed on highly oriented pyrolytic graphite (HOPG). Distribution and atomic sites of 3*d* transition-metal Co nanoislands and adatoms on HOPG were experimentally investigated by scanning tunneling microscopy with atomic resolution. In the very low thickness regime ($\leqslant$0.6 Å), a strong nucleation mechanism and a preferred Co nanoisland diameter of $\sim$3.4 nm have been observed. Co adatoms were found to preferentially occupy $\beta$ sites of the HOPG surface graphene layer and the atoms aggregated by further occupation of either $\alpha$ or overbond sites. This is in contrast to predictions based on density functional theory, which indicates that the hollow sites are the most energetically stable sites for Co adsorption. The presence of surface hydrocarbon contamination on graphite might be one possible cause of the observed active nucleation and stabilized nanoisland diameter of Co. The formation of Co carbide was evidenced by x-ray absorption spectroscopy. More importantly, the Co magnetic spin moment at the interface of Fe-capped ferromagnetic Co nanostructures and graphite, as determined by x-ray magnetic circular dichroism and sum-rule analysis, was found to be only 63% of the bulk value, implying a magnetically defective spin contact for carbon spintronics applications.

DOI: 10.1103/PhysRevB.84.054420 PACS number(s): 85.75.−d, 81.05.uf, 78.70.Dm

## I. INTRODUCTION

Systems comprising interfaces between ferromagnetic metals and materials that are mainly composed of carbon lie at the heart of organic spintronics, which embodies active usage and manipulation of carrier spins in carbon-based materials.[1,2] These materials hold good promise as spin-transport media because of their potentially weak hyperfine and spin-orbit interactions, thus resulting in long spin lifetimes.[3,4] So far, magnetotransport studies have demonstrated spin-valve effects in vertical structures comprising organic semiconductors,[5] and in lateral devices that employ mechanically exfoliated single graphene sheets as spin-transport media.[6–9] In both cases, ferromagnetic electrodes, with or without ultrathin tunnel barriers, are used to generate spin-polarized currents. Karpan *et al.* have put forward a stimulating idea to combine epitaxial sandwich structures containing Co and/or Ni electrodes separated by multilayer graphene and/or graphite.[10] At the epitaxial interfaces of Co (or Ni) and graphene and/or graphite, a perfect spin filtering due to *k*-vector conservation should be possible in theory, relying on the fact that the only states available at the Fermi surface of graphene and/or graphite reside at the *K* points, for which only minority spin states of the ferromagnets are present.[10] When successful, one could expect a new class of spintronic devices similar in layout to magnetic tunnel junctions, but with a carbon-based interlayer replacing the insulating tunnel barrier and, thus, a lower intrinsic resistance area product, which is beneficial, e.g., for current-driven magnetization reversal at low drive voltages.[11,12]

While conceptually very attractive, the practical realization of the epitaxial sandwich structures is a challenging task. To achieve a high spin-filtering efficiency, several (>3) epitaxial graphene layers in the stack are necessary.[10] While the methods for growing *single* layers of lattice-matched graphene on Ni(111) are well established, obtaining graphene multilayers over sufficiently large areas to allow for device fabrication is far more challenging.[13,14] Another difficult task is the fabrication of an *epitaxial* ferromagnetic electrode on top of the multilayer graphene stack. In the case of a fairly large amount of graphene layers, obscuring any influence of the underlying metallic substrate, the growth of the top electrode should be very similar to that on graphite surfaces. Previous studies of the growth of Ni on highly oriented pyrolytic graphite (HOPG) indicate the formation of three-dimensional (3D) Ni(111) islands at 90 K, while clusters lacking a preferred crystallographic orientation were formed at 300 K, the latter representing the thermodynamically stable case.[15] Since graphite forms a very weakly interacting substrate, only strongly out-of-equilibrium conditions might produce epitaxy, otherwise the dominating interactions between the metal atoms is expected to lead to a Volmer-Weber (VW) growth mode.

In this paper, we investigate the initial nucleation and growth of Co nanoislands on HOPG at room temperature (RT) with scanning tunneling microscopy (STM). We monitor the adsorption of individual Co adatoms and ultrasmall clusters (e.g., dimers, trimers) at very low coverages, and compare the results to those of previously published calculations. X-ray absorption spectroscopy (XAS) and x-ray magnetic circular dichroism (XMCD) have been used to probe the magnetic properties at the Co/graphite interfaces, which are not very well established so far in the literature.

## II. EXPERIMENTAL DETAILS

A commercial variable-temperature ultrahigh vacuum (UHV) STM from RHK Technologies was primarily used to characterize the initial nucleation and growth of Co (purity 99.999%) deposited *in situ* on HOPG by *e*-beam evaporation at a rate of 0.2 Å/min in an interconnected custom-made sample preparation chamber. During the deposition, the chamber pressure was maintained below $8 \times 10^{-10}$ mbar. The HOPG substrates (Grade SPI−1, 10 × 10 × 1 mm) were obtained from SPI Supplies. Immediately before insertion into the load-lock chamber, the substrate surface was cleaved along the basal plane by adhesive tape. STM images were acquired in constant

 

current mode using mechanically cut Pt−Ir (90%−10%) tips at RT with a set-point current of 1.0 nA and a bias voltage of 200 mV.

The Co/HOPG samples for XAS measurements were prepared *in situ* at the experimental station with a base pressure of $10^{-10}$ mbar at beam line D1011 of MAX-Laboratory in Lund, Sweden. The C *K*-edge and Co $L_{2,3}$-edge XAS spectra were collected in total-electron-yield mode, where the sample current was recorded as a function of photon energy. To perform XMCD measurements, we used 75% circularly polarized x-rays, which were incident at an angle of 45° with respect to the sample normal. Magnetic fields of up to ±250 Oe were applied along the x-ray propagation direction using an electromagnet. The XMCD signals of the samples were obtained by taking the difference in the absorption intensity measured for the parallel and antiparallel configurations of the x-ray beam helicity and the magnetization direction.

## III. RESULTS AND DISCUSSION

### A. Structural characterization by STM

Figures 1(a)–1(c) display three-dimensional STM images of the same HOPG surface after 0.1, 0.2, and 0.6 Å Co deposition at RT. It is clear from these images that 3D islanding, i.e., the VW mode, is the predominant growth mechanism for Co on HOPG. The 3D island formation can be understood in terms of a large difference in surface energy of Co (2.5 J/m$^2$) (Ref. 16) and HOPG (0.2 J/m$^2$).[17] Metal adatoms deposited onto HOPG surfaces usually possess a high mobility, as they only weakly interact with the surface via Van der Waals interaction. Surface defects such as steps provide nucleation centers and limit adatom mobility due to the presence of broken C–C bonds, thus resulting in a higher density of particles compared to those formed on the substrate terraces. From the STM images, it appears that the nanoislands are dome shaped with a narrow height-to-width aspect ratio of 0.13 to 0.16 for a nominal thickness spanning from 0.1 to 0.6 Å. It should be noted that the true shape of the nanoislands may not be completely resolved due to tip convolution. Nevertheless, it can be inferred unambiguously that the islands do not possess a flat top facet, which would certainly be captured by the STM. For analysis of height and diameter distributions of the islands, many STM images have been measured. The island diameter histograms are depicted in Figs. 1(d)–1(f) and are each fitted with a log-normal distribution function. The error accompanying each mean value $\mu$ corresponds to the standard deviation $\sigma$ derived from the fit. The fact that the mean diameter remains at ∼3.4 nm, despite an increase in the amount of Co, is characteristic of the nucleation-dominated growth regime, where additional deposition predominantly results in the formation of new nuclei on the HOPG surface, and the height of the islands increases very slightly with increasing Co deposition. In Fig. 1(g), we define the Co percentage coverage as the percentage of surface area of a 300 nm × 300 nm scan area being occupied by the adsorbed Co. One can see that the percentage coverage is always below 5%, and the Co island density in the same scan area increases steeply from 5.50 × $10^{11}$ to 2.51 × $10^{12}$ cm$^{-2}$, as the amount of Co increases. It is worth noting that, in our STM images, the Co nanoisland shape is quite uniform. Considering the low Co thickness regime in our experiments [$\leqslant$0.6 Å, i.e., less than approximately 0.35 monolayer (ML) assuming hexagonal close-packed Co], this is in agreement with previously published work by Poon *et al.*, who found that an irregularity of the Co cluster shape started to set in, as the amount of deposited Co was increased from 0.34 to 0.45 ML.[18] Also notable in the log-normal distribution is the relative population of nanoisland sizes, or the skewness, with respect to the mean size. The skewness points towards smaller island diameter for 0.1 and 0.2 Å Co deposition, and varies very slightly towards the mean value for 0.6 Å. The larger abundance of smaller nanoislands than the mean diameter implies active nucleation where island formation is kinetically favored over island growth, as expected in the nucleation-dominated regime. As pointed out also by Poon *et al.*, the origin of such an active nucleation of Co nanostructures on HOPG remains puzzling.[18] Yet, as will be discussed in the next section, the strong nucleation and the stabilization of the Co nanoisland size on HOPG in the very low thickness regime might be triggered and mediated by the presence of residual hydrocarbons on the surface graphene layer of HOPG and the formation of cobalt carbide, which are both revealed in the XAS measurements.

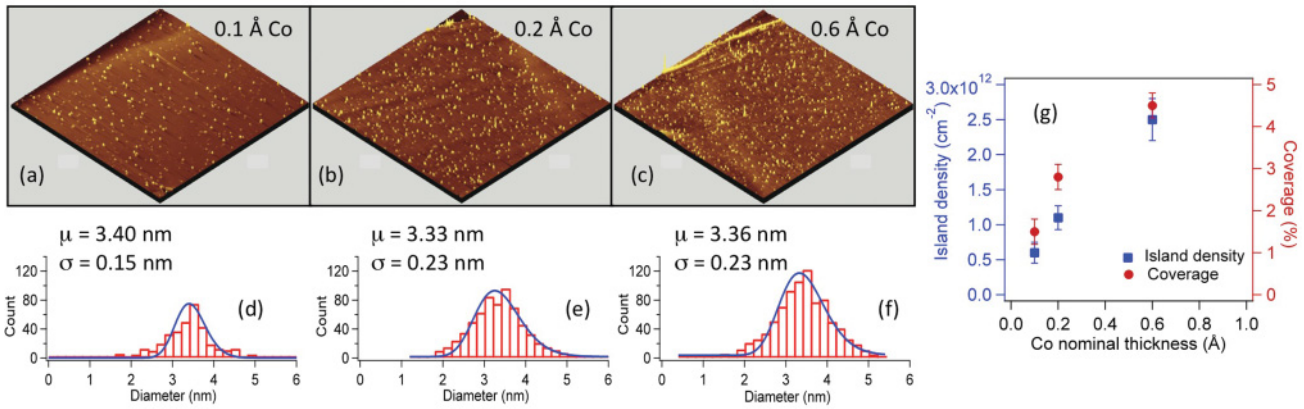


FIG. 1. (Color online) (a)–(c) STM images of Co on HOPG with submonolayer Co coverage. (d)–(f) The island diameter distributions and fitted log-normal distribution functions. (g) The island density profile and the percentage coverage of Co as a function of amount of Co deposited on HOPG at RT.

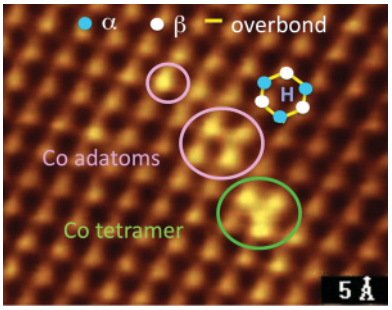


FIG. 2. (Color online) Atomic resolution STM image of Co adatoms adsorbed on HOPG, taken at $I = 1.04$ nA and $V = 219$ mV. The bright spots encircled and labeled as "Co adatoms" refer to individual Co adatoms that were adsorbed on the $\beta$ site of the surface graphene layer, whereas those encircled and labeled as "Co tetramer" correspond to a Co tetramer formed by four Co adatoms. Three of these adatoms occupied the $\beta$ sites and the fourth adatom attached to either the $\alpha$ or the overbond site. The label H indicates the hollow site.

So far, experimental exploration of the nucleation, growth mechanism, and interaction between transition-metal adsorbates and graphene or graphite at the atomic scale remains very limited. The interaction between these dissimilar materials has been investigated mainly by theoretical approaches, such as density functional theory (DFT).[19–23] In the following, we would like to establish practical knowledge of Co adatom adsorption on the different atomic sites of the graphite surface lattice. We believe this important piece of information will be of great interest to other studies regarding the verification of theoretical predictions, as well as the understanding of the influence of ferromagnetic metal contacts on charge and spin transport in graphene or graphite.[6–9] Shown in Fig. 2 is an atomic resolution STM image of the surface graphene layer of HOPG, on which Co adatoms were adsorbed. The trigonal lattice structure clearly observed in the figure presents a typical and perfect superstructure with $\alpha\beta\alpha\beta$ stacking of graphite. It is commonly recognized that $\beta$ site carbon atoms of graphite are usually revealed as bright spots in a STM image and are located just in the centers of the hexagonal carbon rings of the adjacent graphene layer in the hexagonal graphite crystal. The contrast difference between the $\alpha$ and $\beta$ site carbon atoms is due to the existence of interlayer interactions between adjacent graphene layers, which cause an energy dispersion of about 1 eV along the chains of $\alpha$ site atoms normal to the layers. Consequently, a higher local density of states of the $\beta$ site carbon atoms is found near the Fermi level, and therefore, a triangular rather than a honeycomb STM pattern.[24] The closest distance between the $\beta$ site carbon atoms observed in the section analysis of the atomic resolution image is measured to be 0.246 nm, which is in good agreement with previously reported values.[25] More importantly, the STM image directly reveals the mechanisms of Co adatom adsorption and nucleation on the graphite surface: The Co adatoms, which are captured as bright spots on the HOPG, occupy preferentially the $\beta$ sites, labeled $\beta$ in Fig. 2, of the graphite surface lattice. Also illustrated is the way the Co adatoms nucleate locally to form a tetramer, as encircled in Fig. 2. Initially, three Co adatoms bonded to the $\beta$ sites and the fourth adatom occupies either the $\alpha$ or the overbond site, which can not be clearly resolved in the image. At this stage, we can conclude that the surface graphene $\beta$ sites are the most energetically favorable adsorption sites for Co adatoms. In contrast to computational results based on DFT,[19,20,23] there is no evidence from our experimental observations to support the hollow sites (H) being favorable for individual Co atoms to adsorb on. Such disparity between our results and the prediction by the theories might be attributed to the difficulties associated with correctly modeling Van der Waals forces and, thus, binding energies using DFT,[26] which are essential for weakly interacting systems, such as metals on graphene or graphite.

### B. Chemical and magnetic characterization by element-specific XAS and XMCD

Figure 3 shows the C $K$-edge XAS spectra of HOPG as a function of Co deposition time. These spectra have been normalized to the $K$-edge $\pi^*$ peak height to allow for a straightforward comparison of any changes in the spectral features. As one can immediately see, the spectral shape broadens, and a new shoulder, indicated by an arrow in Fig. 3, emerges in the energy range of 282–284 eV, upon increasing Co deposition. The presence of this shoulder has been observed in a number of previous reports and is commonly referred to as a signature of carbide formation. Recently published experimental results obtained by x-ray photoelectron spectroscopy suggest that, instead of the direct interaction between Co and graphite, surface defects,[18,27] hydrocarbon contaminations on graphite surfaces,[18] and minute residual C-containing species even under UHV conditions[18,27] are the main causes for Co–C formation. In the first mechanism, C atoms of surface hydrocarbons dissociate and form new bonds with Co atoms. Combining these spectroscopic data with the STM results described in the preceding section, it is plausible that such a contamination-mediated interfacial interaction is strong enough to bind the Co nanostructures to the HOPG substrate and reduce their surface diffusion, subsequently leading to dominant nucleation as well as the observed uniformity of Co nanoisland dimensions in the growth regime studied here.

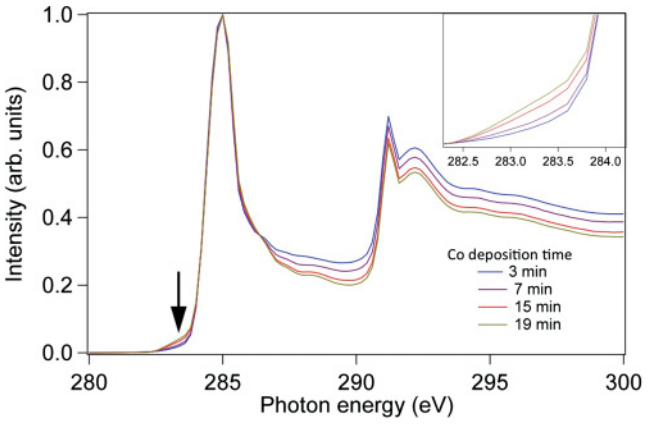


FIG. 3. (Color online) C $K$-edge XAS spectra as a function of Co deposition time. The inset shows the lower energy scale, featuring a new shoulder, as indicated by the black arrow, of which intensity increases with increasing Co deposition time.

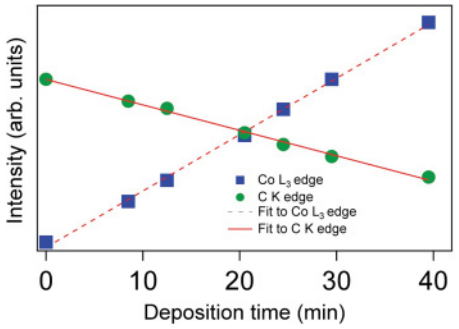


FIG. 4. (Color online) Peak intensity versus Co deposition time profile for C K-edge $\pi^*$ transition peaks and Co $L_3$-edge XAS measurements of Co/HOPG. The linearity shown by the fit of the Co XAS measurements implies the VW growth mode of Co on graphite.

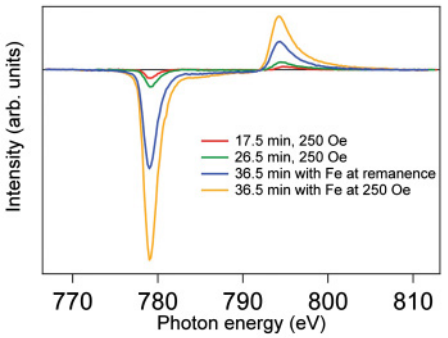


FIG. 5. (Color online) Normalized Co $L_{2,3}$-edge XMCD intensity as a function of Co deposition times and of applied magnetic field during the measurements.

This scenario appears to be even more convincing if one takes into consideration the very recent atomic resolution scanning transmission electron microscopy studies done by Zan *et al.*, where the authors showed that, similar to Fe adatoms, Co adatoms prefer to stick on hydrocarbons on single- and few-layer graphene.[28]

The XAS peak intensity *versus* deposition time profiles of the C *K*-edge and Co $L_3$-edge, shown in Fig. 4, verify the VW growth mode of Co on graphite as observed in our STM characterization, as can be concluded from the linearity of those peaks with the deposition time. Due to the surface sensitivity of XAS, a significant increase in the ratio between bulk and surface Co atoms during growth (as expected, e.g., for a substantially increasing cluster size or a layer-by-layer growth mode) would lead to a nonlinear (saturating) intensity versus coverage behavior. The linear increase of the Co $L_3$-edge signal with deposition time observed here shows that the ratio of bulk-to-surface atoms is approximately constant, in agreement with nucleation-dominated growth. The slow decrease of the C *K*-edge signal from the substrate is due to the relatively high exposure of the substrate surface.

Experimental determination of the magnetic properties of interfaces between ferromagnetic metals and graphene and/or graphite remains practically nonexistent, and provides a special challenge, since a technique, preferably with submonolayer sensitivity and element specificity, would be required. The use of XMCD, which offers these capabilities and simultaneously allows for direct and separate quantitative evaluation of atomic spin and orbital magnetic moments of a given sample, is particularly suited for this purpose.[29–32] Figure 5 illustrates the Co $L_{2,3}$-edge XMCD of the samples with various Co deposition time, normalized to the XAS step height at 815 eV, i.e., well above the $L_2$ edge, where dichroic effects are negligible. It can be seen that the Co nanostructures are free from oxidation, due to the lack of multiplet structure at the Co *L*-edge, and display clear dichroic signals, which increase with increasing Co deposition time, therefore implying an increase in the total magnetic moments of the Co nanostructures. It should be noted that those dichroic effects were observed only when a magnetic field was applied during the measurements, but not at remanence, therefore indicating superparamagnetic (SPM) behavior of the Co nanoislands at RT. We confirmed this by recording the Co XMCD intensity of the samples as a function of the external magnetic field, evidenced in the inset of Fig. 6. Due to the limited field strength that one could apply in the experimental station, the figure solely shows the (nearly linear) middle part of a typical "*S*"-shaped magnetic hysteresis loop of an SPM material. In order to determine the magnetic moments of the Co nanoislands at an elevated temperature and at a relatively weak field, we introduced an Fe layer on top of the Co islands. The Fe layer couples ferromagnetically to the Co islands, thus allowing very low thicknesses of Co on HOPG to become ferromagnetic at RT, thereby effectively simulating the behavior at the interface with a ferromagnetic Co film. This is illustrated by the Fe and Co XMCD loops depicted in Fig. 6. The intensity $M_{\mathrm{XMCD}}$ of the hysteresis loops was determined by measuring the helicity-dependent absorption signals at the maximum of the Fe and Co $L_3$-edge $(\mu_{\mathrm{on}})_{\pm}$ and in the pre-edge region $(\mu_{\mathrm{off}})_{\pm}$, while scanning the external field back and forth, via

$$M_{\mathrm{XMCD}} \propto \frac{(\mu_{\mathrm{on}} - \mu_{\mathrm{off}})_+ - (\mu_{\mathrm{on}} - \mu_{\mathrm{off}})_-}{(\mu_{\mathrm{on}} - \mu_{\mathrm{off}})_+ + (\mu_{\mathrm{on}} - \mu_{\mathrm{off}})_-}. \qquad (1)$$

The normalization to the signal in the pre-edge region is necessary to zero out any artificial magnetic field-dependent (but magnetization-independent) background (see also, e.g., Ref. 33). As shown in the figure, both Fe and Co XMCD loops exhibit identical coercivities and also reveal an overall

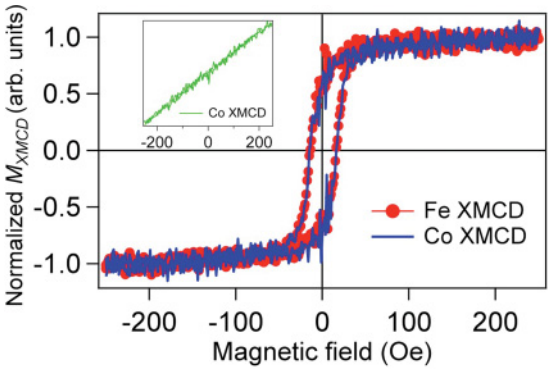


FIG. 6. (Color online) Normalized Co and Fe $L_3$-edge XMCD hysteresis loops of Fe-capped Co/HOPG. The inset shows the SPM Co XMCD loop of bare Co/HOPG at RT.

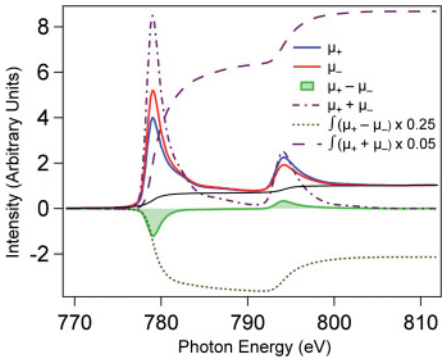


FIG. 7. (Color online) Sum-rule analysis of Co $L_{2,3}$-edge XAS and XMCD spectra of Fe-capped Co/HOPG with a deposition time of 36.5 min measured at RT. The measurements were taken in the presence of a 250-Oe magnetic field. The symbols shown in the figure are explained in the text.

similar shape after a further normalization of the loops to their respective intensity at 250 Oe. More importantly, due to the existence of the Fe cap, the Co hysteresis loop now exhibits a remanence, which is clearly absent in the bare Co/HOPG.

The XMCD sum rules were used to extract the values of orbital and spin magnetic moments from the Fe-capped Co XMCD spectra shown in Fig. 7.[31,34] A magnetic field of 250 Oe was applied in the measurements in order to magnetically saturate the sample. Following the procedure introduced by Chen *et al.*, the "unstructured absorption" was simulated by a simple two-step background and subtracted from the absorption spectra for computing the $2p$ to $3d$ XAS intensities $\mu_+$ and $\mu_-$ for parallel and antiparallel alignment of photon helicity and magnetization.[30] Then, the orbital $m_{\mathrm{orb}}$ and spin magnetic moments $m_{\mathrm{spin}}$ were obtained from the integrals of the total XAS $\int(\mu_+ + \mu_-)$ and XMCD $\int(\mu_+ - \mu_-)$ spectra for calculating the values for $p$, $q$, and $r$ (see Ref. 30), using the following sum rules:

$$m_{\mathrm{orb}} = -4qn_h/3rP, \tag{2}$$

$$m_{\mathrm{spin}} = (4q - 6p)n_h/rP. \tag{3}$$

The number of holes $n_h$ was taken as 2.29 for Co (Ref. 30) and the degree of polarization $P$ was 0.75. The results of the sum-rule analysis, compared to the bulk values, are described in Table I. As shown, the spin moment of the Co nanoislands is $1.01\pm0.13\ \mu_B$, representing 63% of the bulk value.[30] This reduction might be a direct consequence of the aforementioned Co–C formation. In contrast to the reduction in spin moment, the orbital moment shows a remarkable enhancement of 140% with respect to the bulk value. This orbital enhancement is possibly originating from (1) a reduced delocalization-induced quenching of the orbital moment in nanoclusters, and (2) the reduction of symmetry in comparison with the bulk structure, which can change the orbital degeneracy.[32]

TABLE I. Spin and orbital magnetic moments in units of $\mu_B$ per atom of Co on HOPG and bulk hcp Co.

| Structure | $m_{\mathrm{orb}}/\mu_B$ | $m_{\mathrm{spin}}/\mu_B$ | $m_{\mathrm{orb}}/m_{\mathrm{spin}}$ |
|---|---|---|---|
| Co/HOPG | $0.218 \pm 0.027$ | $1.01 \pm 0.13$ | $0.216 \pm 0.026$ |
| Bulk Co (Ref. 30) | 0.154 | 1.62 | 0.095 |

In terms of the lattice-matched spin-filtering interfaces proposed by Karpan *et al.*, where FM/graphite interfaces are basic building blocks,[10] the results obtained by our structural and magnetic characterizations would suggest that such epitaxial interfaces can not be obtained straightforwardly with conventional approaches. Although epitaxial interfaces of Co and graphene were only very recently demonstrated by Vo-Van *et al.* using pulsed-laser deposition, the control over the produced Co crystal phase in their ultrathin films remains lacking, making this task seemingly insurmountable at present.[35] Spin transport in graphene has already been demonstrated and accomplished by several groups,[6–9] but the quality and magnetic robustness of the spin contacts adopted in these experiments, however, remain relatively unexplored. Of high relevance to our magnetic characterization results is the case where spin contacts are fabricated by direct intimate contacts between Co and single-layer graphene, as utilized by Han *et al.*[7,36] Due to the reduced spin moments of Co in the presence of hydrocarbon contaminations on surfaces of graphene or graphite, one would expect that the initially injected spin polarization in the vicinity of the Co/(graphene or graphite) interfaces will not be optimal.

## IV. CONCLUSIONS

In summary, structural investigation of the transition-metal Co on highly oriented pyrolytic graphite by STM revealed that Co atoms and nanoislands nucleate actively on graphite, in apparent disagreement with the known noninteracting nature of the carbon material. This behavior might be attributed to the hydrocarbon surface contamination on the surface graphene of HOPG, which causes Co carbide formation, as clearly evidenced in the XAS spectra. Using XMCD, the interface magnetic properties of nanostructured Co/graphite have been studied. This was made possible by the inclusion of a ferromagnetic Fe cap atop the SPM Co nanoislands, which facilitated the determination of the spin and orbital moments at the hybrid interface at moderate magnetic field strength. The measurements reveal a 40% reduction and a 140% enhancement in the spin and orbital moments, respectively, when compared to the bulk. It is likely that our results might give an insight into the issues, such as the magnetic integrity of spin injection and detection contacts that are made of $3d$ transition ferromagnetic metals and (single-) few-layer graphene, without a tunnel barrier, for carbon spintronics.

## ACKNOWLEDGMENTS

We would like to thank A. Preobrajenski of MAX-lab for technical assistance in the XAS and XMCD measurements and H. Zandvliet for useful discussions. The research leading to these results has received funding from the European Commission Seventh Framework Programme (FP7/2007-2013) under Grant Agreement No. 228424 Project MINOTOR.

*m.p.dejong@utwente.nl

[1]W. J. M. Naber, S. Faez, and W. G. van der Wiel, J. Phys. D: Appl. Phys. **40**, R205 (2007).
[2]V. A. Dediu, L. E. Hueso, I. Bergenti, and C. Taliani, Nat. Mater. **8**, 707 (2009).
[3]D. Huertas-Hernando and A. Brataas, Phys. Rev. B **74**, 155426 (2006).
[4]B. Trauzettel, D. V. Loss, and G. Burkard, Nat. Phys. **3**, 192 (2007).
[5]Reference 2 and references therein.
[6]N. Tombros, C. Jozsa, M. Popinciuc, H. T. Jonkman, and B. J. van Wees, Nature (London) **448**, 571 (2007).
[7]W. Han, W. H. Wang, K. Pi, K. M. McCreary, W. Bao, Y. Li, F. Miao, C. N. Lau, and R. K. Kawakami, Phys. Rev. Lett. **102**, 137205 (2009).
[8]C. Jozsa, M. Popinciuc, N. Tombros, H. T. Jonkman, and B. J. van Wees, Phys. Rev. Lett. **100**, 236603 (2008)
[9]W. Han, K. Pi, K. M. McCreary, Y. Li, J. J. I. Wong, A. G. Swartz, and R. K. Kawakami, Phys. Rev. Lett. **105**, 167202 (2010).
[10]V. M. Karpan, G. Giovannetti, P. A. Khomyakov, M. Talanana, A. A. Starikov, M. Zwierzycki, J. van den Brink, G. Brocks, and P. J. Kelly, Phys. Rev. Lett. **99**, 176602 (2007)
[11]S. Mangin, D. Ravelosona, J. A. Katine, M. J. Carey, B. D. Terris, and E. E. Fullerton, Nat. Mater. **5**, 210 (2006).
[12]C. Chappert, A. Fert, and F. Nguyen Van Dau, Nat. Mater. **6**, 813 (2007).
[13]J. M. Garcia, R. He, M. P. Jiang, J. Yan, A. Pinczuk, Y. M. Zuev, K. S. Kim, P. Jim, K. Baldwin, K. W. West, and L. N. Pfeiffer, Solid State Commun. **150**, 809 (2010).
[14]A. Reina, X. Jia, J. Ho, D. Nezich, H. Son, V. Bulovic, M. S. Dresselhaus, and J. Kong, Nano Lett. **9**, 30 (2009).
[15]M. Bäumer, J. Libuda, and H. –J. Freund, Surf. Sci. **327**, 321 (1995).
[16]M. Aldén, H. L. Skriver, S. Mirbt, and B. Johansson, Surf. Sci. **315**, 157 (1994).
[17]M. E. Schrader and G. I. Loeb, *Modern Approaches to Wettability: Theory and Applications* (Plenum, New York, 1992).
[18]S. W. Poon, J. S. Pan, and E. S. Tok, Phys. Chem. Chem. Phys. **8**, 3326 (2006).
[19]D. M. Duffy and J. A. Blackman, Phys. Rev. B **58**, 7443 (1998).
[20]C. Cao, M. Wu, J. Z. Jiang, and H.-P. Cheng, Phys. Rev. B **81**, 205424 (2010).
[21]G. M. Wang, J. J. BelBruno, S. D. Kenny, and R. Smith, Surf. Sci. **541**, 91 (2003).
[22]K. T. Chan, J. B. Neaton, and M. L. Cohen, Phys. Rev. B **77**, 235430 (2008).
[23]Y. L. Mao, J. M. Yuan, and J. X. Zhong, J. Phys. Condens. Matter **20**, 115209 (2008).
[24]D. Tománek, S. G. Louie, J. Mamin, D. W. Abraham, R. E. Thompson, E. Ganz, and J. Clarke, Phys. Rev. B **35**, 7790 (1987).
[25]J. Xhie, K. Sattler, M. Ge, and N. Venkateswaran, Phys. Rev. B **47**, 15835 (1993).
[26]O. Leenaerts, B. Partoens, and F. M. Peeters, Phys. Rev. B **77**, 125416 (2008).
[27]G.-X. Zhang, D. Q. Yang, and E. Sacher, J. Phys. Chem. C **111**, 17200 (2007).
[28]R. Zan, U. Bangert, Q. Ramasse, and K. S. Novoselov, Nano. Lett. **11**, 1087 (2011).
[29]W. L. Brien and B. P. Tonner, Phys. Rev. B **50**, 12672 (1994).
[30]C. T. Chen, Y. U. Idzerda, H.-J. Lin, N. V. Smith, G. Meigs, E. Chaban, G. H. Ho, E. Pellegrin, and F. Sette, Phys. Rev. Lett. **75**, 152 (1995).
[31]B. T. Thole, P. Carra, F. Sette, and G. van der Laan, Phys. Rev. Lett. **68**, 1943 (1992).
[32]G. van der Laan, Phys. Rev. Lett. **82**, 640 (1999).
[33]E. Goering, A. Fuss, W. Weber, J. Will, and G. Schütz, J. Appl. Phys. **88**, 5920 (2000).
[34]P. Carra, B. T. Thole, M. Altarelli, and X. D. Wang, Phys. Rev. Lett. **70**, 694 (1993).
[35]C. Vo-Van, Z. Kassir-Bodon, H. Yang, J. Coraux, J. Vogel, S. Pizzini, P. Bayle-Guillemaud, M. Chshiev, L. Ranno, V. Guisset, P. David, V. Salvador, and O. Fruchart, New J. Phys. **12**, 103040 (2010).
[36]W. Han, K. Pi, W. Bao, K. M. McCreary, Y. Li, W. H. Wang, C. N. Lau, and R. K. Kawakami, Appl. Phys. Lett. **94**, 222109 (2009).